



HAL
open science

Spectral analysis of dispersed multiphase flows in the presence of fluid interfaces

Gabriel Ramirez, Alan Burlot, Rémi Zamansky, Guillaume Bois, Frédéric Risso

► **To cite this version:**

Gabriel Ramirez, Alan Burlot, Rémi Zamansky, Guillaume Bois, Frédéric Risso. Spectral analysis of dispersed multiphase flows in the presence of fluid interfaces. 2023. hal-04295313v2

HAL Id: hal-04295313

<https://hal.science/hal-04295313v2>

Preprint submitted on 17 Apr 2024 (v2), last revised 14 Oct 2024 (v4)

HAL is a multi-disciplinary open access archive for the deposit and dissemination of scientific research documents, whether they are published or not. The documents may come from teaching and research institutions in France or abroad, or from public or private research centers.

L'archive ouverte pluridisciplinaire **HAL**, est destinée au dépôt et à la diffusion de documents scientifiques de niveau recherche, publiés ou non, émanant des établissements d'enseignement et de recherche français ou étrangers, des laboratoires publics ou privés.



Distributed under a Creative Commons Attribution 4.0 International License

Spectral analysis of dispersed multiphase flows in the presence of fluid interfaces

Gabriel Ramirez^{a,b}, Alan Burlot^b, Rémi Zamansky^a, Guillaume Bois^b,
Frédéric Risso^{a,*}

^a*Institut de Mécanique des Fluides de Toulouse (IMFT), Université de Toulouse and
CNRS, Toulouse, France*

^b*Université Paris-Saclay, CEA, Service de Thermo-hydraulique et de Mécanique des
Fluides, 91191, Gif-sur-Yvette, France*

Abstract

Spectral analysis of dispersed two-phase flows is highly desirable to reveal the interplay of the various flow scales, much larger or much smaller than the size of the dispersed bodies. This is a challenging task as the matching conditions at the body interfaces generate singularities in the fields describing the two-phase mixture. The nature of these singularities and their consequences on the spectra are theoretically analyzed for bubble or droplet flows. Results of direct numerical simulations are reported and spatial spectra of the mixture velocity, the flow forces and their power are examined. The regular part of the spectral densities of energy production, dissipation and transfers between scales are separated from their singular part. The resulting spectral energy balance, free of the footprint of the singularities, is found in agreement with coarse-grained simulations where the interfaces are filtered out before solving the Navier-Stokes equations. These results pave the way for the spectral analysis of more complex turbulent dispersed flows.

Keywords: Dispersed Flows, Bubbles, Droplets, Turbulence,
Body-Induced-Agitation, Spectral Analysis

*Corresponding author
Email address: frisso@imft.fr (Frédéric Risso)

1. Introduction

The dynamics of dispersed multiphase flows are controlled by the interactions between a population of bodies - either droplets, bubbles or solid particles - and a fluid phase in which they are randomly distributed. The bodies have a great impact on flow fluctuations either by modulating a pre-existing shear-induced turbulence (Balachandar and Eaton, 2010; Brandt and Coletti, 2022) or by directly inducing agitation through their motion relative to the fluid (Risso, 2018). Spectral analysis is a powerful tool to understand turbulence, since two-point correlations give access to the flow structure. Applied to multiphase flows, it should reveal the interplay between scales and lead to a better modeling. In particular, our objective is to determine the spectral density of the power of all the forces that contribute to the energy balance, distinguishing between rate of production, dissipation and transfer between scales. However, the question of how to achieve this in the presence of numerous sharp interfaces between the carrier and dispersed phases is not trivial.

Since the pioneering work of Lance and Bataille (1991), many experimental works have reported one-dimensional spectra of the liquid phase velocity in bubbly flows. Different methods were used to deal with the interruptions by the bubbles: removing the parts of the signal belonging to the gas phase and filling the gaps by a smooth function (Lance and Bataille, 1991), retaining only parts of the signals between two bubbles which are not interrupted (Martínez Mercado et al., 2010; Mendez-Diaz et al., 2013; Roghair et al., 2011; Prakash et al., 2016; Alméras et al., 2017), measuring the flow just behind a rising bubble swarm (Riboux et al., 2010). A few numerical studies have proposed spectral analysis of the velocity field of the carrying phase in order to make direct comparisons with experiments (Roghair et al., 2011). However, spectra obtained from Direct Numerical Simulations (DNS) of dispersed two-phase flows are generally calculated by considering the entire flow field without distinguishing between carrying and dispersed phases (Tryggvason et al., 2002; Lucci et al., 2010; Dodd and Ferrante, 2016; Pandey and Ramadugu, 2020; Innocenti et al., 2021; Pandey

31 et al., 2022; Crialesi-Esposito et al., 2022).

32 The question of whether the spectral analysis should take into account the
33 entire flow mixture or only the carrying phase deserves to be discussed. In this
34 work, we focus on numerical simulations where the flow is known everywhere and
35 consider the case of a statistically homogeneous dispersed flow in a large periodic
36 domain, which is well suited to a spectral description in the \mathbf{k} -wavenumber
37 domain.

38 We examine first the option of building spectra of the continuous phase only,
39 and immediately set aside the method of filling the region occupied by the dis-
40 persed phase by an arbitrary smooth field. Considering a region of the flow that
41 is never crossed by an interface ensures that the field of any physical quantity
42 is smooth. However, the surface of the bodies are now boundaries from which
43 momentum and energy are supplied to the system under study. All the local
44 statistical quantities, such as velocity variance, energy dissipation rate, pres-
45 sure gradient or inertial forces, depend on the distance to those boundaries. In
46 such a heterogeneous flow, an average spatial spectrum $S(\mathbf{k})$ cannot represent
47 a meaningful spectral density of any of these fields. This would make no more
48 sense than constructing a spatial spectrum from the velocity along a line per-
49 pendicular to a wall in a channel flow. An attempt to overcome this limitation
50 has been done by Freund and Ferrante (2019) who analyzed DNS results of a
51 droplet laden flow. They used wavelets, a tool developed to deal with inho-
52 mogeneous fields by allowing the construction of spectra, $S(\mathbf{x}, \mathbf{k})$, that depend
53 also on the location \mathbf{x} . For each wavenumber, the domain was decomposed
54 into three regions in contact but without intersections: an intermediary region
55 I crossed by the interfaces, a region C fully located in the continuous phase
56 and a region D fully located in the droplets. Vector \mathbf{x} was only used to deter-
57 mine to which region belongs a given point and three spectra, $S_I(\mathbf{k})$, $S_C(\mathbf{k})$ and
58 $S_D(\mathbf{k})$, one for each region, were calculated. Since the spectra depend only on
59 \mathbf{k} , they still face the inconsistency of describing highly heterogeneous fields. A
60 more sophisticated use of wavelets preserving the double dependency in \mathbf{x} and
61 \mathbf{k} could lead to a relevant description, but has yet to be developed for the study

62 of dispersed multiphase flows. In this work, we stay with the conclusion that,
63 in the context of a homogenized description based on spectra depending only
64 on the wavenumber, it is not relevant to consider the flow field of the carrying
65 phase only.

66 The remaining option is to consider the flow of the entire mixture. Since
67 it is statistically homogeneous, the use of the Fourier transform is appropriate.
68 However, the fields of the physical quantities under investigation experience
69 singularities at the interfaces between the phases. These singularities are due
70 to the presence of jumps across the interface of some physical properties, such
71 as density and viscosity, and to surface tension. They are of several kinds,
72 such as the discontinuities of the velocity derivatives or the Dirac delta function
73 that describes the pressure gradient. These singularities may have a strong
74 footprint on the spectra. In particular, they can generate oscillations, which
75 were very early reported on the velocity spectra of dispersed two phase flows
76 with large bubbles (Tryggvason et al., 2002) or solid particles (Lucci et al., 2010).
77 These oscillations are associated with the Gibbs phenomenon, familiar in signal
78 processing, and well exemplified by the sine cardinal function, which is the
79 Fourier transform of a gate. Their signature also contains a power-law decay at
80 large wavenumbers, which must not be confused with a dynamical phenomenon
81 (Risso, 2011). The spectra of any flow-field quantity contains a regular part
82 that describes the smooth variations in the bulk phases and a singular part that
83 accounts for interfacial singularities.

84 In what follows, we focus on droplets or bubbles in a fluid, which means that
85 the dynamics of the two phases are described by the Navier-Stokes equations
86 and the interface by an interfacial tension. A similar analysis could be carried
87 out for solid particles in a fluid, but it is out of the scope of the present work.
88 Our objective is to examine the consequences of the presence of interfacial sin-
89 gularities on spectra. The singular part of a spectrum is sometimes qualified
90 as spurious, since it complicates the physical interpretation. However, in the
91 context of the analysis of the mixture fields, it is a part of the mathematical
92 solution of the physical problem. The possibility of separating the regular and

93 singular part is a central question that motivates this work.

94 This paper is organized as follows. Section 2 presents the dynamics equa-
95 tions of the mixture flow and examines the nature of the different interfacial
96 singularities. Section 3 analyzes the spectral signatures of basic singularities
97 caused by droplet or bubble interfaces. Section 4 reports results of direct nu-
98 merical simulations and discusses the spectral density of the velocity, of the
99 terms of the Navier-Stokes equations and of the terms of the energy balance.
100 Section 5 compares with results of coarse-grained simulations, where interfacial
101 singularities are filtered out before solving the Navier-Stokes equations. Sec-
102 tion 6 summarizes the main findings and concludes.

103 **2. Equations of motion of a two-phase mixture and field singularities**

104 In this section, we examine the nature of the singularities encountered by
105 the fields describing the flow, which are due to the presence of fluid interfaces.

106 We decided to analyze the spectral distribution of the entire mixture. For
107 this reason, we write the equations of motion of the fluids as a single set of
108 partial differential equations for the velocity \mathbf{u} and pressure P , which is valid
109 throughout both phases. This means that the matching of the dynamic condi-
110 tions between the two phases at the interfaces have to be inserted within the
111 Navier-Stokes equations for the mixture. Because that matching involves jumps
112 of stresses through the interfaces, the use of generalized functions (Gelfand and
113 Shilov, 1964), known as distributions, is required. Note that this approach is
114 known as one-fluid sharp interface methods in the context of numerical simula-
115 tions of two-phase flow (Kataoka, 1986; Lalanne et al., 2015).

116 We consider a population of fluid particles, either drops or bubbles, dispersed
117 in another fluid. The two fluids are immiscible and form a two-phase mixture,
118 without phase change. The interfaces between the phases are massless, of zero
119 thickness and entirely characterized by a surface tension σ . The density and
120 viscosity of the two fluids are different, but constant in each phase. In the
121 following, the carrier phase, dispersed phase and interfaces are distinguished by

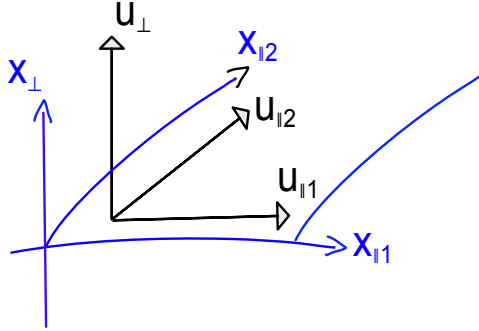


Figure 1: Local coordinates nearby an interface

122 the subscripts c , d and s , respectively. We introduce the indicator function, χ ,
 123 which is equal to one in the dispersed phase and to zero in the carrying phase.
 124 The density ρ and the viscosity μ of the mixture can be written:

$$\rho = \rho_c + (\rho_d - \rho_c)\chi, \quad (1)$$

$$\mu = \mu_c + (\mu_d - \mu_c)\chi. \quad (2)$$

125 In the context of continuum mechanics, in the absence of phase change, the
 126 velocity field is continuous. The mass conservation is

$$\partial_t \rho + \nabla \cdot (\rho \mathbf{u}) = D_t \rho + \rho \nabla \cdot \mathbf{u} = 0. \quad (3)$$

127 Because ρ is constant in each phase and no fluid particle crosses interfaces,
 128 the material derivative ($D_t = \partial_t + \mathbf{u} \cdot \nabla$) of the density is zero and the velocity
 129 field is divergence-free: $\nabla \cdot \mathbf{u} = 0$. This result has further consequences for the
 130 differentiability of \mathbf{u} . Let's consider a portion of the interface and name $x_{\parallel 1}$ and
 131 $x_{\parallel 2}$ the local coordinates along the interface, and x_{\perp} the coordinate orthogonal
 132 to it (fig. 1). Since \mathbf{u} is continuous across the interface, the four strain-rate
 133 components $\partial_{\parallel \xi} u_{\parallel \eta}$ (with ξ and η equal to 1 or 2) are equal on both sides of the
 134 interface and thus have no discontinuity. Then, considering that $\nabla \cdot \mathbf{u} = 0$, we
 135 get that the normal strain rate $\partial_{\perp} u_{\perp} = -\partial_{\parallel 1} u_{\parallel 1} - \partial_{\parallel 2} u_{\parallel 2}$ is continuous too.
 136 Thus, the only derivatives of \mathbf{u} that can present a discontinuity are the shear-
 137 rate components $\partial_{\perp} u_{\parallel \xi}$, the regularity of which is prescribed by the shear-stress

138 matching across the interface and will be discussed later.

139 The momentum equations are formally written as the classic Navier-Stokes
 140 equations with a non-constant viscosity in which surface tension is taken into
 141 account by adding an interfacial force:

$$-\rho D_t \mathbf{u} - \nabla P + \rho \mathbf{g} + \nabla \cdot (2\mu \mathbf{S}) + \mathbf{F}_\sigma = 0, \quad (4)$$

142 where $\mathbf{S} = \frac{1}{2}(\nabla \mathbf{u} + \nabla \mathbf{u}^T)$ is the strain-rate tensor. The interfacial force is written
 143 as

$$\mathbf{F}^\sigma = -\sigma \nabla^S \cdot \mathbf{n} \nabla \chi + \nabla^S \sigma \int_{\mathbf{x}_s} \delta_{3D}(\|\mathbf{x} - \mathbf{x}_s\|) dS, \quad (5)$$

144 where \mathbf{n} is unit normal to the interface pointing outward from the dispersed
 145 phase, ∇^S is the two-dimensional gradient operator on the interface, \mathbf{x}_s is any
 146 point on the interface S and $\delta_{3D}(\|\mathbf{x} - \mathbf{x}_s\|) = \delta(x - x_s)\delta(y - y_s)\delta(z - z_s)$ with
 147 δ the Dirac delta function. The surface divergence $\nabla^S \cdot \mathbf{n}$ of the normal vector
 148 is twice the mean curvature κ of the interface and the gradient of the indicator
 149 function can also be written in terms of the Dirac delta function as

$$\nabla \chi = -\mathbf{n} \int_{\mathbf{x}_s} \delta_{3D}(\|\mathbf{x} - \mathbf{x}_s\|) dS. \quad (6)$$

150 The first term of eq. 5 corresponds to the interfacial jump of the normal stress
 151 due to the capillary pressure: $-2\sigma\kappa$. The second term accounts for the interfa-
 152 cial jump of the shear stress due to the Marangoni effect: $\partial_{\|\xi}\sigma$.

153 Let us examine the nature of the singularities of various fields of interest. A
 154 field V can be decomposed in a regular singularity-free part V_{reg} and interfacial
 155 jumps $[V_{irreg}^{(p)}]$ of its successive derivatives of order p :

$$V(\mathbf{x}) = V_{reg}(\mathbf{x}) + \sum_{p \geq p_{min}}^{p_{max}} [V_{irreg}^{(p)}(\mathbf{x} = \mathbf{x}_s)], \quad \text{with } p_{min} \geq -1. \quad (7)$$

156 The integer p_{min} is the order of the lowest derivative that is discontinuous, which
 157 characterizes the strongest singularity of V . The sum may continue to infinity
 158 or stop at a finite value p_{max} , which then characterizes the less sharp singularity.
 159 At this point, it is worth mentioning that the regularity of the solutions of the
 160 Navier-Stokes equations is a very hard mathematical issue, which is still an

	Regular part	$p \geq 1$ (continuous)	$p = 0$ Heaviside type	$p = -1$ Dirac type
Buoyancy: $\rho \mathbf{g}$	✓		✓	
Inertia: $-\rho D_t \mathbf{u}$	✓		✓	
Interfacial force: \mathbf{F}_σ				✓
Pressure gradient: $-\nabla P$	✓	?	✓	✓
Viscous diffusion: $\nabla \cdot (2\mu \mathbf{S})$	✓	?	✓	✓ if $\mu_c \neq \mu_d$ or $\nabla^S \sigma \neq 0$

Table 1: Interfacial discontinuities (eq. 7) involved in each terms of the momentum equations (eq. 4). A check mark means that the corresponding discontinuity-type is present.

161 open question even in the case of a single-phase flow (Onsager, 1949; Duchon
162 and Robert, 2000; Dubrulle, 2019). As the aim of the present work is to examine
163 the practical consequences of the presence of fluid interfaces on the spectra of
164 the fields, we shall concentrate on the lower values of p , which correspond to the
165 more severe singularities with the strongest consequences. Note that $p_{min} = 1$
166 corresponds to a field that is continuous whereas its derivative experiences a
167 jump across the interface. Handling values of p that are less than unity means
168 that we consider the word “derivative” in a broader sense. Indeed, we have
169 to deal with the cases where the function itself is discontinuous ($p_{min} = 0$) or
170 is the derivative of a discontinuous function ($p_{min} = -1$). For instance, χ , as
171 well as ρ and μ , is a pure step function of Heaviside type, characterized by
172 $p_{min} = p_{max} = 0$.

173 Table 1 lists the type of discontinuities which are expected to be involved in
174 the various terms of the momentum equations, according to the decomposition
175 defined by eq. 7. For the balance to be satisfied, every singularity appearing in
176 one term of the momentum equations must cancel out with singularities of the
177 same order in the other terms. In other words, the sum of the terms in each
178 column must be zero. We examine now the volume forces of the momentum

179 equations one by one.

180 The buoyancy force $\rho\mathbf{g}$ is the product of the density and the acceleration of
181 gravity; it is thus of pure Heaviside type. Check marks are therefore present
182 only in the columns corresponding to the regular part and the $p = 0$ singularity.

183 Since a fluid particle never crosses an interface and the velocity is continuous,
184 its acceleration $D_t\mathbf{u}$ is expected to be regular. However, because it involves the
185 density, the nature of the singularity of the inertial force $\rho D_t\mathbf{u}$ is the same as
186 that of the buoyancy force.

187 Eqs. 5-6 show that \mathbf{F}^σ is of pure Dirac type and associated with $p_{min} =$
188 $p_{max} = -1$. A check mark is therefore present only in the $p = -1$ column. Note
189 that this is the only term without a regular part, as it is not defined outside the
190 interfaces.

191 The pressure gradient has generally both Heaviside and Dirac singularities.
192 This is easy to show by considering the elementary case of an interface of con-
193 stant σ between two fluids at rest in a constant gravity field: for example a
194 droplet pending at the tip of a capillary tube. Eq. 4 simplifies to

$$\nabla P = -\rho\mathbf{g} - 2\sigma\kappa\nabla\chi, \quad (8)$$

195 where the pressure gradient has to balance both the Heaviside-type buoyancy
196 force and the Dirac-type interfacial force. The first corresponds to the jump in
197 the hydrostatic pressure: $\partial P_d/\partial z - \partial P_c/\partial z = -(\rho_d - \rho_c)g$. The second accounts
198 for the Laplace pressure jump: $P_d - P_c = -2\kappa\sigma$.

199 As regards the viscous force, $\nabla \cdot (2\mu\mathbf{S})$, the fact that the viscosity, which is
200 discontinuous, appears under a differential operator immediately suggests the
201 presence of a Dirac-type singularity. However, it is interesting to analyze its
202 significance by distinguishing again between the tangential and normal direc-
203 tions, and by considering its two possible origins, namely: a viscosity jump or
204 a Marangoni stress.

205 As we have shown before, $\partial_\perp u_\perp$ is continuous across the interface. Therefore,
206 the jump of the normal viscous stress through the interface is equal to $2(\mu_d -$
207 $\mu_c)\partial_\perp u_\perp$. This means that the existence of a viscosity difference between the

208 phases is sufficient to generate a finite jump in the viscous stress, which leads
 209 the viscous volume force in the momentum equation to include a Dirac-type
 210 contribution. The matching of the normal stresses at interface is written

$$2(\mu_d - \mu_c)\partial_\perp u_\perp + (P_d - P_c) + 2\kappa\sigma = 0, \quad (9)$$

211 which shows that even in the case of vanishing surface tension, a jump in viscos-
 212 ity is sufficient to generate a pressure jump. On the other hand, when $\nabla^S\sigma \neq 0$,
 213 the Marangoni stress is responsible for a jump in the tangential shear stress.
 214 Finally, it thus turns out that the viscous volume force contains a Dirac-type
 215 singularity ($p_{min} = -1$) if either $\mu_d - \mu_c \neq 0$ or $\nabla^S\sigma \neq 0$. Since the pressure
 216 gradient involves a Heaviside-type discontinuity ($p = 0$), we can expect that the
 217 viscous force also does so to satisfy the equilibrium of the normal stresses at
 218 the interface under flow conditions. Then, as we have no argument for deciding
 219 whether or not the second (and higher) derivative of the viscous stress should
 220 be the same on both sides of the interface, we have added question marks in the
 221 $p \geq 1$ columns of pressure gradient and viscous force.

222 To end this section, we conclude with the velocity field. We have already
 223 shown that all partial derivatives of u are continuous except the shear-rate
 224 components $\partial_\perp u_{\parallel\xi}$. Therefore, if $\mu_d - \mu_c = 0$ and $\nabla^S\sigma = 0$, the continuity of
 225 the shear stress ensures that of the shear-rate, so all the velocity derivatives are
 226 continuous and \mathbf{u} is characterized by $p_{min} \geq 2$. Otherwise, in the general case,
 227 $p_{min} = 1$.

228 **3. Spectral signatures of basic singularities caused by droplet or bub-** 229 **ble interfaces**

230 In this section we examine the spectral signature of singularities of various
 231 orders p encountered in multiphase flows. For a more general discussion of
 232 spectral analysis of signal with singularities, the reader is referred to (Broer and
 233 Takens, 1993; Bacry et al., 1993; Pikovsky et al., 1995). The energy density
 234 spectrum E_V of a scalar field $V(\mathbf{x})$ is defined as follows. First, we take the

235 three dimensional Fourier transform of $V(\mathbf{x})$:

$$\widehat{V}(\mathbf{k}) = \int e^{i\mathbf{k}\cdot\mathbf{x}} V(\mathbf{x}) d\mathbf{x}. \quad (10)$$

236 Second, we multiply it by its complex conjugate (*), sum over shells \mathcal{A}_w of
237 constant $\|\mathbf{k}\|$ and take the average:

$$E_V(k) = \langle \int_{\|\mathbf{w}\|=k} \widehat{V}(\mathbf{w}) \cdot \widehat{V}^*(\mathbf{w}) d\mathcal{A}_w \rangle, \quad (11)$$

238 (depending on whether V is a scalar or a vector, the operation “.” is a multi-
239 plication of numbers or a scalar product).

240 3.1. Analytical results for spherical interfaces

241 We introduce the indicator function $\mathcal{H}_{\text{sphere}}$ of a ball (interior of a sphere)
242 as a reference Heaviside-type field, and the indicator function δ_{sphere} of a sphere
243 (surface of a ball) as a Dirac-type field. These fields are respectively representa-
244 tive of the density and the interfacial force of a two-phase mixture of spherical
245 droplets. Their Fourier transforms are

$$\widehat{\mathcal{H}}_{\text{sphere}}(\mathbf{k}) = \frac{4\pi}{\|\mathbf{k}\|^3} (\sin(R\|\mathbf{k}\|) - R\|\mathbf{k}\|\cos(R\|\mathbf{k}\|)) \quad (12)$$

246 and

$$\widehat{\delta}_{\text{sphere}}(\mathbf{k}) = \frac{4\pi R}{\|\mathbf{k}\|} \sin(R\|\mathbf{k}\|) \quad (13)$$

247 where R is the sphere radius (Gelfand and Shilov, 1964). Their spectra are

$$E_{\mathcal{H}_{\text{sphere}}}(k) = \frac{(4\pi)^2}{k^4} (\sin(Rk) - Rk \cos(Rk))^2, \quad (14)$$

248 and

$$E_{\delta_{\text{sphere}}}(k) = (4\pi R)^2 \sin^2(Rk). \quad (15)$$

249 The spectra of the two cases present oscillations of period $k_b = \pi/R$, correspond-
250 ing to $\sin^2(Rk)$. On the one hand, the oscillations of $E_{\delta_{\text{sphere}}}$ keep constant phase
251 and amplitude for all k . On the other hand, $E_{\mathcal{H}_{\text{sphere}}}$ behaves as $R^6 k^2$ at small
252 k and as $k^{-2} \cos^2(Rk)$ at large k , which means it cancels out for both $k = 0$ and
253 $k = \infty$.

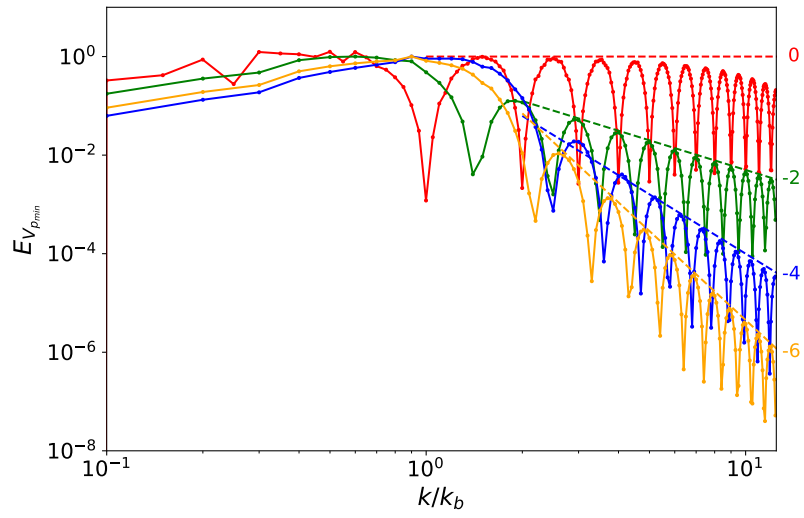


Figure 2: Numerical spectra of three-dimensional scalar fields of various singularity orders: $p_{min} = -1$ (red), $p_{min} = 0$ (green), $p_{min} = 1$ with $J_1 = 1$ (blue), $p_{min} = 2$ with $J_2 = 10$ (orange). The dashed straight lines correspond to $k^{-2-2p_{min}}$, with the exponent written on right side.

254 *3.2. Numerical results for spherical interfaces*

255 We have numerically computed the spectra of basic singular scalar fields
 256 $V_{p_{min}}$, characterized by a value p_{min} from -1 to 2, defined as follows:

$$V_{-1}(\mathcal{X}) = \delta(\mathcal{X}), \quad (16)$$

$$V_0(\mathcal{X}) = \mathcal{H}(\mathcal{X}), \quad (17)$$

$$V_1(\mathcal{X}) = (\mathcal{X}^2 - 1)((J_1/2 + 1)\mathcal{X}^2 - 1)\mathcal{H}(\mathcal{X}), \quad (18)$$

$$V_2(\mathcal{X}) = (\mathcal{X}^2 - 1)^2((J_2/8 - 1)\mathcal{X}^2 + 1)\mathcal{H}(\mathcal{X}), \quad (19)$$

257 where $\mathcal{H}(\xi)$ is the classic Heaviside function (equal to zero for $\xi < 0$ and to
 258 one for $\xi > 0$), \mathcal{X} is the normalized distance from the surface of the sphere:
 259 $\mathcal{X} = 1 - \|\mathbf{x} - \mathbf{x}_c\|/R$. V_{-1} and V_0 correspond to δ_{sphere} and $\mathcal{H}_{\text{sphere}}$. Then, it is
 260 easy to check that V_1 and V_2 have the expected level of singularity provided J_1
 261 and J_2 are finite. Indeed, both are regular inside the sphere and zero outside,
 262 while at the interfaces: $V_1 = 0$ and V_1' undergoes a jump J_1 ; $V_2 = V_2' = 0$
 263 and V_2'' undergoes a jump J_2 . (In contrast with δ_{sphere} and $\mathcal{H}_{\text{sphere}}$, V_1 and
 264 V_2 do not correspond to a pure singularity of order $p = 1$ or 2 , which means
 265 that $p_{max} \neq p_{min}$.) These four fields have been mapped on a three-dimensional
 266 regular grid of spacing $\Delta = R/25$, which implies that numerical interfaces have a
 267 non zero thickness. Then, the spectrum of each of them is computed numerically
 268 by making use of the discrete Fourier transform.

269 Fig. 2 shows the spectra of V_{-1} , V_0 , V_1 and V_2 as functions of the wavenumber
 270 k normalized by k_b . The numerical spectrum of δ_{sphere} is in agreement with the
 271 analytical result (eq. 15), except at large k where the numerical approximation of
 272 the delta function becomes rough. However, the numerical spectrum of $\mathcal{H}_{\text{sphere}}$
 273 remains accurate beyond $k = 10k_b$, so we can trust as well the numerical spectra
 274 of V_1 and V_2 in the considered range of wavenumbers.

275 The conclusions obtained from the analytical expressions of $E_{\delta_{\text{sphere}}}$ and
 276 $E_{\mathcal{H}_{\text{sphere}}}$ can be generalized to larger values of p_{min} . All spectra show oscil-
 277 lations of period k_b and a final power-law decay. At wavenumbers much smaller
 278 than $1/R$, they all show a similar pattern and behave as k^2 as k tends towards

279 zero. At large k , the spectrum behaves as $k^{-2p-2} \sin^2(R\|\mathbf{k}\| + \phi)$. At this stage,
 280 two main conclusions can be drawn. On the one hand, the decay is controlled
 281 by the order of the singularity: the more regular the function, the lower p_{min} ,
 282 the faster the decay. On the other hand, the period of the oscillations and the
 283 wavenumber where the singularity spectrum is maximum are controlled by the
 284 droplet size, whatever the nature of the discontinuity.

285 The power-law decay generated by an interface singularity of a field should
 286 not be confused with the power-law subrange exhibited by a regular physical
 287 field, such as the inertial $k^{-5/3}$ of single-phase flow turbulence or the k^{-3} of
 288 bubble-induced agitation (Lance and Bataille, 1991; Risso, 2018). Such physi-
 289 cal subranges always have a cutoff at a certain wavenumber: the Kolmogorov
 290 microscale in the case of turbulence (Pope, 2000), the size of smaller bubble
 291 disturbances in the model of bubble-induced spectrum by Risso (2011). A sin-
 292 gularity power-law never stops and always exceeds the regular part of a physical
 293 signal at large wavelengths.

294 At scales close to the size of a droplet, the question of which one dominates
 295 in a physical signal between the regular part or the singularity has no general
 296 answer and must be examined in each specific situation.

297 *3.3. Effects of deviation from sphericity and of interface thickness*

298 In real situations, droplets or bubbles are often not spherical. Also, spatial
 299 resolution is finite, which means that a fluid interface can never be described
 300 by a surface of zero thickness. In particular, numerical simulations based on
 301 the sharp-interface formulation have to deal with finite-size meshes that contain
 302 the two phases. In this section, we examine the consequences on the spectrum
 303 of a singularity of the drop non-sphericity, defined by an aspect ratio a/b , and
 304 of a finite interface thickness, ϵ_s . In what follows, R is defined as the radius of
 305 a sphere of the same volume and all calculations have been performed on the
 306 same mesh as that used in the previous section.

307 We begin with the case of the Heaviside singularity ($p_{min} = 0$). Figure 3
 308 shows numerical spectra E_{V_0} obtained by considering an oblate ellipsoidal in-

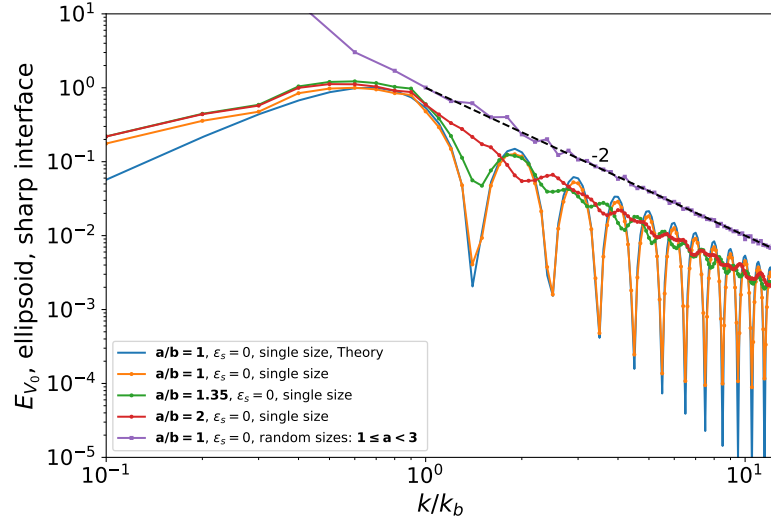


Figure 3: Numerical spectra of the indicator function of oblate ellipsoidal balls ($p_{min} = 0$, Heaviside type) of single size with various aspect ratios a/b or spherical balls with random sizes. The dashed line corresponds to $k^{-2p_{min}-2}$.

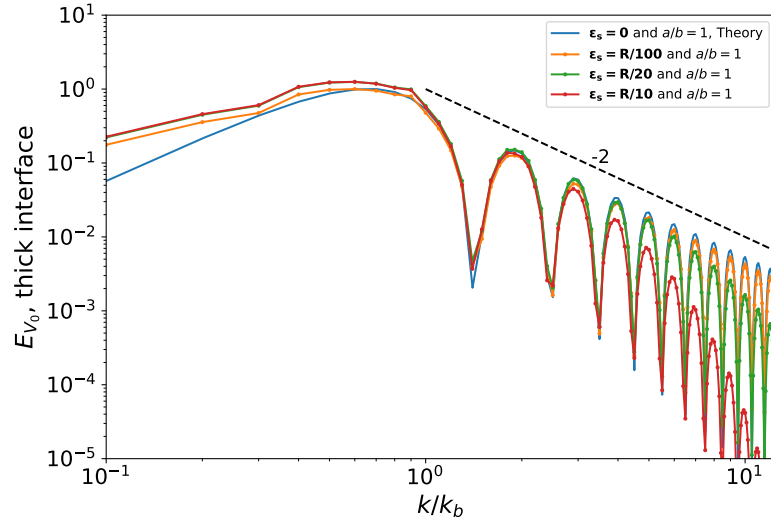


Figure 4: Numerical spectra of the indicator function of spherical balls ($p_{min} = 0$, Heaviside Type) with smooth interface of various thicknesses ϵ_s . The dashed line corresponds to $k^{-2p_{min}-2}$.

309 terface with $a/b = 1.35$ and 2 , which is still sharp ($\epsilon_s = 0$), together with
 310 the theoretical result (eq. 15) and the numerical result for a sphere (fig. 2).
 311 Deformation clearly dampens oscillations, and the greater a/b , the lower the
 312 oscillation amplitude. This is easily understood by noting that, for an ellip-
 313 soid, the distance 2β between two diametrically opposed points on the interface
 314 varies between $2a$ and $2b$ depending on the direction considered. The three-
 315 dimensional spectrum therefore mixes oscillations of various periods π/β , which
 316 cannot remain in phase as k increases, causing them to cancel each other out.
 317 Figure 3 also shows the spectrum computed by considering spherical interfaces
 318 of random radii uniformly distributed between R and $3R$. One sees that a simi-
 319 lar damping of the oscillations occurs when one considers a population of drops
 320 of different sizes, with the variation of R from drop to drop substituting for the
 321 variation of 2β with direction. In any case, this process has no effect on the
 322 baseline of the spectrum, the decays of which remains the same.

323 Figure. 4 presents numerical E_{V_0} obtained by considering a spherical in-
 324 terface of finite thickness. The interface has been smoothly extended over a
 325 thickness ϵ_s by replacing the Heaviside function in eq. 17 by an error function:
 326 $V_0(\mathcal{X}) = 1 - \{\text{erf}[(\mathcal{X} - 1)/\epsilon_s]\}/2$. For $\epsilon_s = R/100$, the interface thickness is
 327 below the grid resolution $\Delta = R/25$, and the numerical result is the same as
 328 that of fig. 3, and in agreement with the theory. The effect of ϵ_s becomes visible
 329 when it becomes larger than Δ . A finite thickness affects the small scales by
 330 increasing the final decay of the spectrum, without having any effect on the
 331 oscillations. However, it has no impact on the scales that are much larger than
 332 ϵ_s . This means that a very strong localized gradient of a regular field, such as
 333 that of the velocity in a large-Reynolds number boundary layer of thickness ϵ_{BL}
 334 around a drop, would generate a similar spectral signature as a velocity jump
 335 at scales much larger than ϵ_{BL} . We can also wonder whether singularities as-
 336 sociated with intermittency (Le Berre et al., 2023) could also affect turbulence
 337 spectra in a similar way.

338 Now, we examine the case of the Dirac singularity ($p_{min} = -1$). The Dirac
 339 delta function in eq. 16 is replaced by finite boxcar function of height ϵ_s and

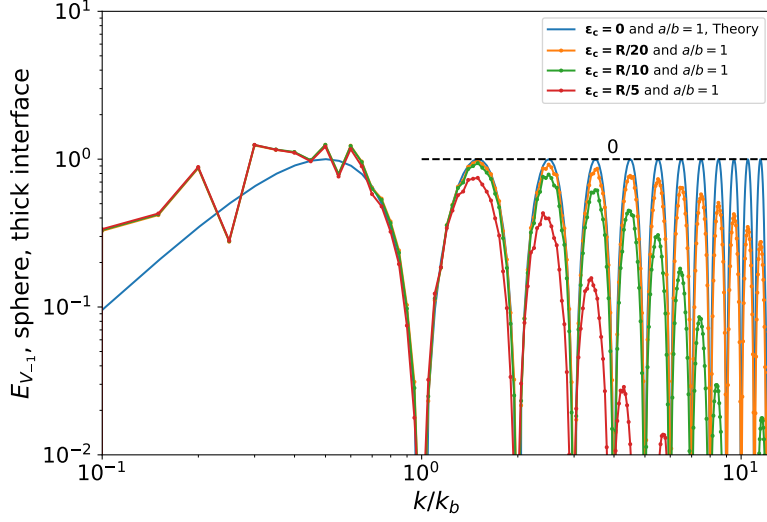


Figure 5: Numerical spectra of the indicator function of spheres ($p_{min} = -1$, Dirac type) of various thicknesses ϵ_s . The dashed line corresponds to $k^{-2p_{min}-2}$.

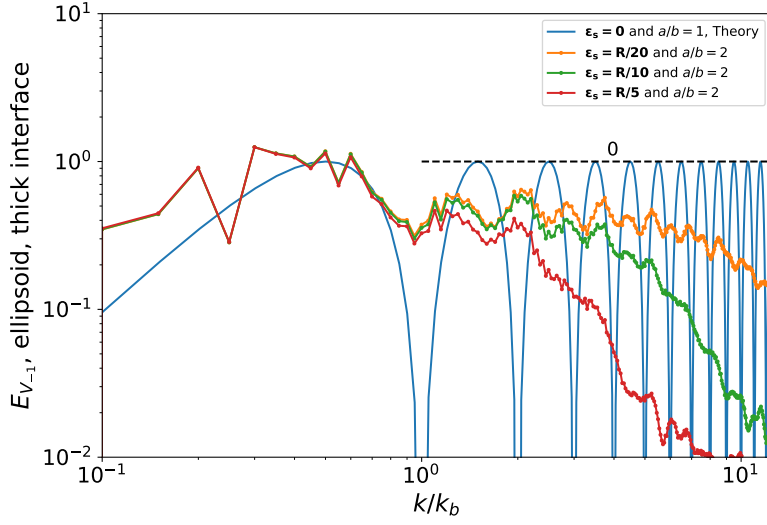


Figure 6: Numerical spectra of the indicator function of an oblate ellipsoid ($p_{min} = -1$, Dirac type, $a/b = 2$) with a smooth interface of various thicknesses ϵ_s . The dashed line corresponds to $k^{-2p_{min}-2}$.

340 width $1/\epsilon_s$. Figure 5 shows the numerical spectra for spherical interfaces of
 341 various thicknesses, while fig. 6 shows the same results for oblate ellipsoids of
 342 aspect ratio $a/b = 2$. The conclusions are the same as for the Heaviside singu-
 343 larity. Increasing the interface thickness causes a faster decay of the spectrum
 344 at large wavenumber. Increasing the deformation generates a damping of the
 345 oscillations.

346 *3.4. Spectral signatures of singularities in physical cases*

347 We showed in the previous section (eq. 2) that a finite jump in the fluid prop-
 348 erties (density or viscosity) across the interface or a non-zero interfacial tension
 349 causes singularities in the fields that characterize the flow. In the present section,
 350 we examined the signature of basic singularities of various orders corresponding
 351 to fluid interfaces of droplets. For spherical drops having all the same radius
 352 R , the spectrum of the interface singularities is maximum close to $k_b = \pi/R$,
 353 shows oscillations of period k_b and decays at small scales as k^{-2p-2} . For poly-
 354 disperse or deformed drops the oscillations may be absent, while the baseline of
 355 the singularity spectrum is still present.

356 A real physical field is more complex, since it includes a contribution from
 357 the regular part that accounts for the dynamics in the bulk phases, in addition
 358 to singular contributions that account for the interfaces. Is it possible to dis-
 359 tinguish between the regular and the singular parts? First of all, we may try to
 360 attribute the presence of oscillations as $\sin^2(kR + \phi)$ to the singular part. This
 361 first approach has two limitations. On the one hand, for drops moving at large
 362 Reynolds number relative to the carrying phase, oscillations may be due to the
 363 presence of a dynamic boundary layer at the drop surface. On the other hand,
 364 spectra calculated from DNS of highly deformed drops with a broad size dis-
 365 tribution immersed in a turbulent field by Crialesi-Esposito et al. (2022) show
 366 no oscillations, for the reason explained above. Secondly, we can rely on small
 367 scales to detect the singular part. In principle, the singular part undergoes a
 368 never-ending power-law decay as k approaches infinity. It must therefore even-
 369 tually emerge from the regular part, which has a physical cutoff, corresponding

370 to the Kolmogorov microscale in a turbulent flow. However, the dissipative
371 range is most of the time not resolved, which means that we need to detect the
372 singular contribution at larger scales.

373 At this stage, it is therefore difficult to anticipate a general method for
374 distinguishing the regular part from the singular part, which would probably
375 have to be done on a case-by-case basis. Furthermore, even if such a distinction
376 can be made, the question of its physical relevance remains open.

377 **4. Direct numerical simulations of bubble-induced agitation**

378 In the previous section, we examined the theoretical consequences of basic
379 jump conditions on the spectrum of some reference fields. We are now interested
380 in analyzing their practical effects on the spectrum of physical fields, such as
381 the mixture velocity and the volume forces involved in the momentum balance.
382 Since the spectrum of interface discontinuities is significant for wavelengths of
383 the order of the drop size R and smaller, it has negligible consequences when
384 most of the energy is contained at scales much larger than R , as in the case
385 of droplets or bubbles smaller than the Kolmogorov microscale in a turbulent
386 field. On the other hand, the case of a swarm of rising bubbles in an otherwise
387 quiescent fluid is particularly impacted, since the energy of the fluctuations is
388 generated by the bubbles at scales close to R .

389 The fluid velocity in both phases can hardly be measured in experiments.
390 Most of the time, only the velocity field of the outer phase is measured in two-
391 phase dispersed flows. In addition, the flow in the close vicinity of bubbles
392 or droplets is often removed because of spurious measurements. On the other
393 hand, DNS using sharp interface methods provide exhaustive information on all
394 physical fields at any location. In what follows, we analyze in detail the results
395 of DNS of a homogeneous swarm of bubbles rising at high Reynolds number.

396 *4.1. Presentation of the simulations*

397 Bubbles having all the same size are initially homogeneously distributed
398 over a triperiodic cubic domain and then rise under the action of buoyancy.

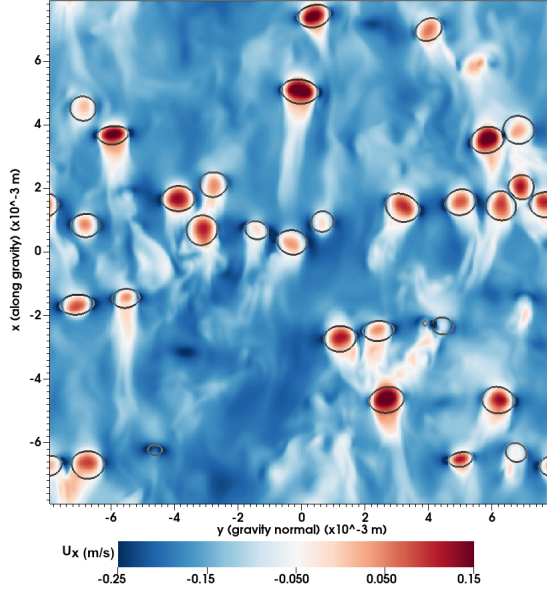


Figure 7: Snapshot showing the vertical velocity in a vertical plane ($\alpha = 6\%$, refined mesh)

399 After an initial transient, the flow statistics cease to evolve in time. All sub-
 400 sequent results are obtained in this statistically steady state. The simulations
 401 are carried out with the open-source TRUST/TrioCFD code, which uses of a
 402 front-tracking method to solve the continuity and Navier-Stokes equations in
 403 the sharp-interface form (eqs. 3, 4) across the entire domain, including both
 404 the gas and liquid phases. The code has been described in detail and validated
 405 for high-Reynolds-number bubbly flow with parameters similar to those of the
 406 present work in du Cluzeau et al. (2019, 2022).

407 The physical parameters are: $\mu_c = \mu_d = 3.73 \times 10^{-4}$ Pa.s, $\rho_c = 1.1713 \times$
 408 10^3 kg/m³, $\rho_d = 87.545$ kg/m³, $\sigma = 18.05 \times 10^{-3}$ N/m, $d = 2R = 10^{-3}$ m,
 409 $g = 9.81$ m/s². This gives an Archimedes number $Ar = \frac{\rho_c d \sqrt{(1 - \rho_d / \rho_c) g d}}{\mu_c} \approx 300$
 410 and a Bond number $Bo = (\rho_c - \rho_d) g d^2 / \sigma \approx 0.6$, corresponding to slightly
 411 deformed bubbles in a flow regime dominated by inertia. The density ratio,
 412 $\rho_d / \rho_c \approx 1/13$, and viscosity ratio, $\mu_d / \mu_c = 1$, are outside the range expected for

413 bubbly flow at common room temperature and pressure. Note also that surface
414 tension is kept constant. These conditions have been chosen to simplify the
415 entanglement of the various singularities in the analysis of the spectrum of the
416 various terms. In particular, the theoretical analysis suggests that a viscosity
417 ratio equal to unity should ensure a more regular velocity and, together with a
418 constant σ , to a more regular viscous force.

419 The simulations are performed on a 432^3 regular mesh in a cubic domain
420 of side $L = 31.7 \times 10^{-3}$ m or $L = 15.85 \times 10^{-3}$ m. In the larger domain, the
421 mesh-grid spacing is thus $\Delta = 73.5 \times 10^{-6}$ m, while in the smaller domain it is
422 $\Delta = 36.77 \times 10^{-6}$ m.

423 Two gas volume fractions have been considered: $\alpha = 0.03$ and 0.06 . A
424 snapshot of the flow is shown in fig. 7. The case $\alpha = 0.03$ has been solved
425 on the larger domain ($L = 32d$) with the lower resolution ($\Delta = d/14$). It
426 gives the following overall statistics for the two-phase mixture: average bubble
427 relative velocity $u_r = 0.17$ m/s, half the variance of the mixture velocity $K_m =$
428 $5.4 \times 10^{-2} u_r^2$ and dissipation rate per unit volume $\epsilon_m = 7.45 \times 10^{-3} \rho_c u_r^3/d$.
429 The average bubble Reynolds number, Weber number and aspect ratio are:
430 $Re = \frac{\rho_c d u_r}{\mu_c} = 528$, $We = \frac{\rho_c d u_r^2}{\sigma} = 1.83$ and $a/b = 1.39$.

431 The case $\alpha = 0.06$ has been solved on both the larger domain ($L = 32d$,
432 $\Delta = d/14$) and the smaller domain with a better resolution ($L = 16d$, $\Delta =$
433 $d/27$). The lower resolution gives: $u_r = 0.150$ m/s, $K_m = 11.2 \times 10^{-2} u_r^2$,
434 $\epsilon_m = 18.5 \times 10^{-3} \rho_c u_r^3/d$, $Re = 470$, $We = 1.45$ and $a/b = 1.33$. The greater
435 resolution gives: $u_r = 0.147$ m/s, $K_m = 11.8 \times 10^{-2} u_r^2$, $\epsilon_m = 22.0 \times 10^{-3} \rho_c u_r^3/d$,
436 $Re = 462$, $We = 1.40$ and $a/b = 1.37$. Rigorously, even our finest resolution is
437 not enough to exactly capture the boundary layer around the bubbles at such
438 a Reynolds number (Innocenti et al., 2021), which explains small differences
439 between the two resolutions. In the literature, such a limitation is encountered
440 in many numerical simulations involving a large number of dispersed particles.
441 This is not a serious limitation for the aim of the present work, which is to
442 analyze the spectral signature of interface discontinuities, as we shall see later
443 when comparing the results of our coarse and refined meshes.

444 *4.2. Spectrum of density and velocity*

445 In a numerical simulation, even in the case where the mesh grid is fitted
446 to follow the interface, the fields are described with a finite resolution Δ . The
447 consequences for the spectrum have been discussed in section 3.3 where an
448 interface of finite thickness has been considered. A coarser resolution leads to a
449 faster decrease in the spectral footprint of the singularities. In addition, with the
450 front tacking method used here, the two-dimensional mesh that describes the
451 interface differs from the three-dimensional one on which is discretized the bulk
452 flow. In a cell containing both phases, the values of the density and viscosity
453 have to be interpolated between those of the two phases, as it is also the case
454 with common other sharp-interface methods, such as VOF or Level-Set. Here
455 the density is determined as the arithmetic mean of the densities of the two
456 phases weighted by their volume fraction within the cell considered. Since the
457 viscosity is assumed constant, no interpolation is required. The interfacial force
458 is computed from the curvature of the two-dimensional interface mesh. Then,
459 \mathbf{F}_σ is distributed over the cells of the three-dimensional mesh that are located at
460 a distance lower than Δ from the interface. Therefore, the Dirac delta function
461 is smoothed over a width of approximately 2Δ .

462 The effect of a region where the mixture is described by a fluid with in-
463 termediate properties can hardly be anticipated, but it may redistribute the
464 singularities between the different terms of the momentum balance in a way
465 that probably depends on the numerical scheme.

466 Let us consider first the consequences of the numerical discretization on the
467 spectra of two basic fields: the density ρ , which is only impacted by the finite
468 resolution, and the velocity u , which is affected by both the finite resolution and
469 by the way the continuity and Navier-Stokes equations are solved. Note that
470 the spectra are normalized by using k_b and their variance $\langle\langle(\cdot)^2\rangle\rangle$, in order to ease
471 comparison between the two volume fractions.

472 Figure 8 shows the spectrum of the density for the three different simulations
473 and the analytical solution $E_{\mathcal{H}_{\text{sphere}}}$ (eq. 14). Whatever the volume fraction or
474 the resolution, the spectrum shows oscillations as $\sin^2(Rk)$ in agreement with

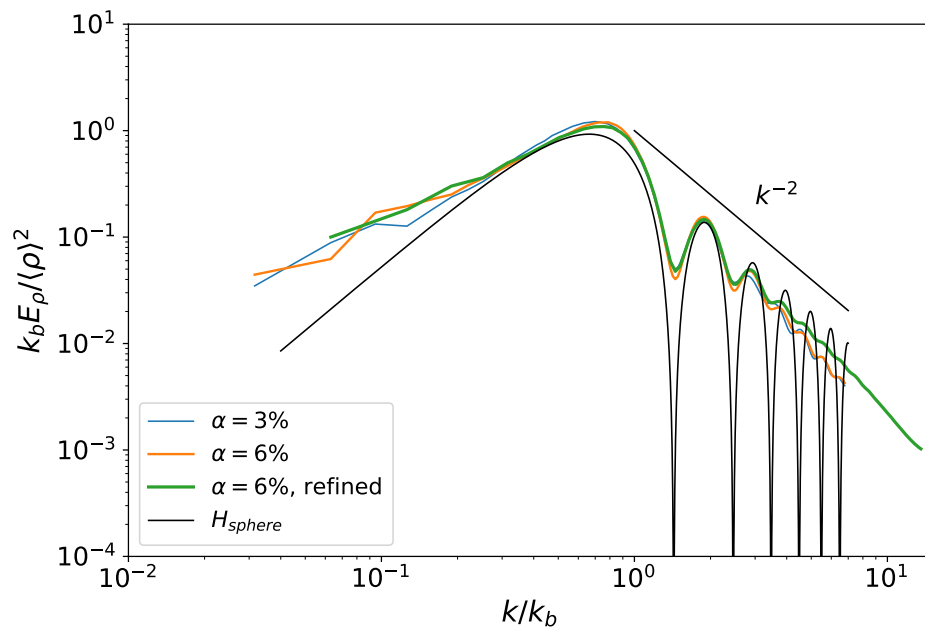


Figure 8: Normalized spectrum of the density (DNS results). The straight line shows the asymptotic evolution $k^{-2p_{min}-2}$, with $p_{min} = 0$.

475 the analytical solution. Oscillation amplitudes are smaller due to departure
 476 from sphericity. Cases $\alpha = 3\%$ and $\alpha = 6\%$ at the coarser resolution match at
 477 all wavenumbers and agree at large scales with the case at finer resolution. The
 478 coarser cases show a decay in agreement with the theoretical k^{-2} up to $k = 3k_b$,
 479 while the finer case follows it up to $6k_b$, showing that halving the mesh spacing
 480 actually halves the scale from which the interface begins to be seen as less sharp
 481 than it should be. Regarding the density, the numerical spectrum behaves as
 482 predicted by the theory.

483 Figure 9 shows the spectrum E_u of the velocity. The spectra of the three
 484 cases are very similar, featuring oscillations with a period k_b . We note only
 485 differences at very large scales due to finite domain size, and at very small scales
 486 close to the Nyquist wavenumber. This indicates that the velocity spectrum is
 487 very robust to changes in resolution. The spectrum reaches a maximum near k_b ,
 488 followed by a k^{-3} subrange, which is known as a signature of the bubble-induced
 489 agitation (Risso, 2018). Then, it shows a steeper decay as k^{-4} for $k > 3k_b$,
 490 followed by an even steeper one as k^{-n} , with $4 < n < 5$, for $k > 6k_b$. Under
 491 present conditions, with no viscosity jump or interfacial tension gradient, the
 492 predictions for u are $p_{min} = 2$, which corresponds to a final decay as k^{-6} . The
 493 fact that u is less regular than expected is probably a consequence of numerical
 494 approximations in the cells crossed by the interface.

495 4.3. Spectrum of the terms of the momentum equations

496 We examine now the spectra of the five terms involved in the momentum
 497 balance (4) from the DNS at $\alpha = 6\%$ with either the coarse or the refined
 498 resolution: buoyancy $(\rho - \rho_m)\mathbf{g}$, interfacial force \mathbf{F}_σ , pressure gradient $-\nabla P$,
 499 inertia $-\rho D_t \mathbf{u}$ and viscous diffusion $\nabla \cdot (2\mu \mathbf{S})$. Note that $\rho_m = (1 - \alpha)\rho_c + \alpha\rho_d$ is
 500 the average mixture density and we have chosen to include the mean hydrostatic
 501 pressure gradient $\rho_m \mathbf{g}$ in the buoyancy term so that it takes into account all the
 502 external forces acting on the two-phase system. In this section, all spectra are
 503 normalized using k_b and the variance of $(\rho - \rho_m)\mathbf{g}$. It is worth recalling that
 504 the spectrum is quadratic in the quantity considered, so that the balance of the

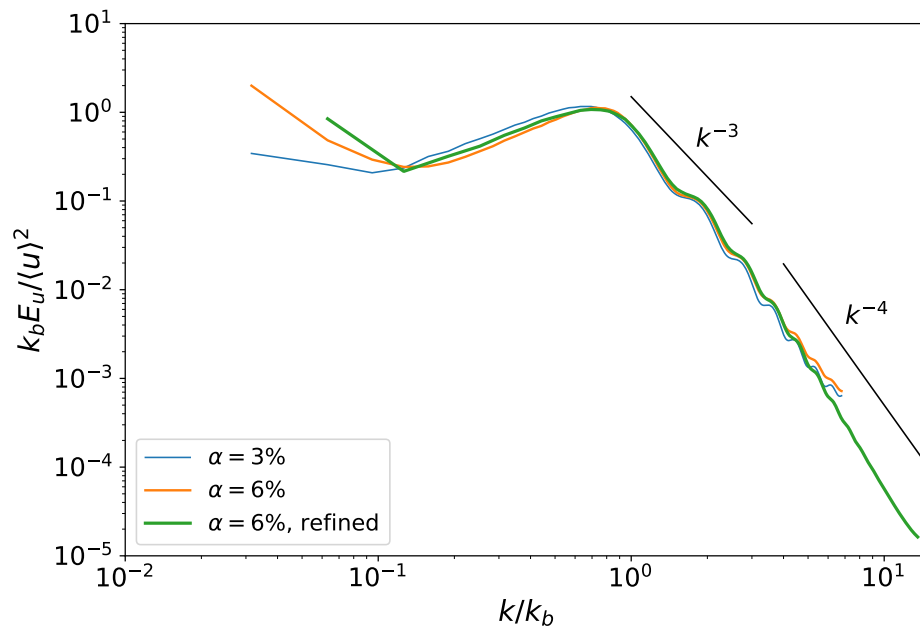


Figure 9: Normalized spectrum of the velocity (DNS results). Note that the expected final decay is k^{-6} ($p_{min} = 2$) for the case without viscosity jump.

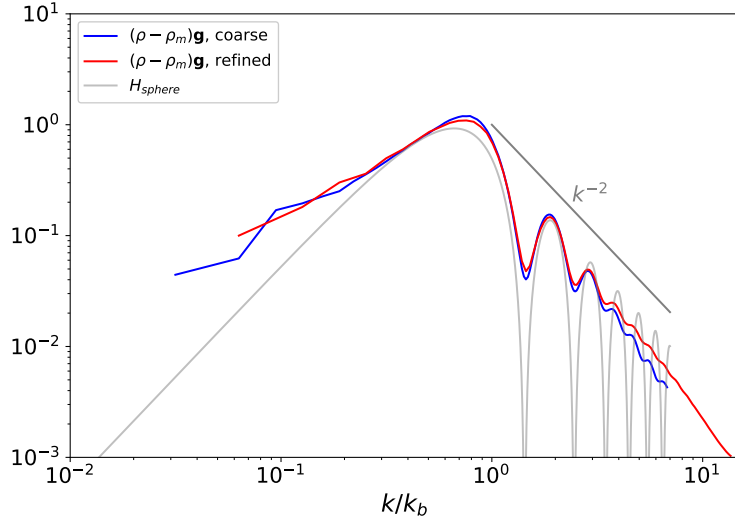


Figure 10: Normalized spectrum $E_{(\rho - \rho_m)\mathbf{g}}$ of buoyancy force at $\alpha = 6\%$ (DNS results)

505 five terms does not lead to a simple constraint on their spectra. When only two
 506 terms are in equilibrium, their spectrum is the same, but it is not as simple for
 507 more terms.

508 Since \mathbf{g} is constant, the spectrum of $(\rho - \rho_m)\mathbf{g}$ (fig. 10) is similar to that of
 509 ρ (fig. 8) and leads to the same conclusions.

510 Figure 11 presents the spectra of \mathbf{F}_σ and $-\nabla P$. At large scales, for wavenum-
 511 bers smaller than $\approx 2k_b$, both are independent of the mesh refinement. At small
 512 scales, the Dirac-type singularity introduced by interfacial tension gives a con-
 513 stant intensity. We indeed observe a plateau of the baseline before a cut-off due
 514 to the finite resolution, which appears at a smaller k at lower resolution. Still,
 515 at small scales, the spectra of \mathbf{F}_σ and $-\nabla P$ are identical, which confirms that
 516 the Dirac-type singularities cancel out entirely between the interfacial force and
 517 the pressure gradients, in agreement with the equilibrium of normal stresses at
 518 the interface. The theoretical spectra $E_{\mathcal{H}_{\text{sphere}}}$ and $E_{\delta_{\text{sphere}}}$ are also reported. It
 519 turns out that the oscillations of the pressure gradient are in phase with $E_{\mathcal{H}_{\text{sphere}}}$
 520 at large scales and with $E_{\delta_{\text{sphere}}}$ at small scales, which underlines the fact that

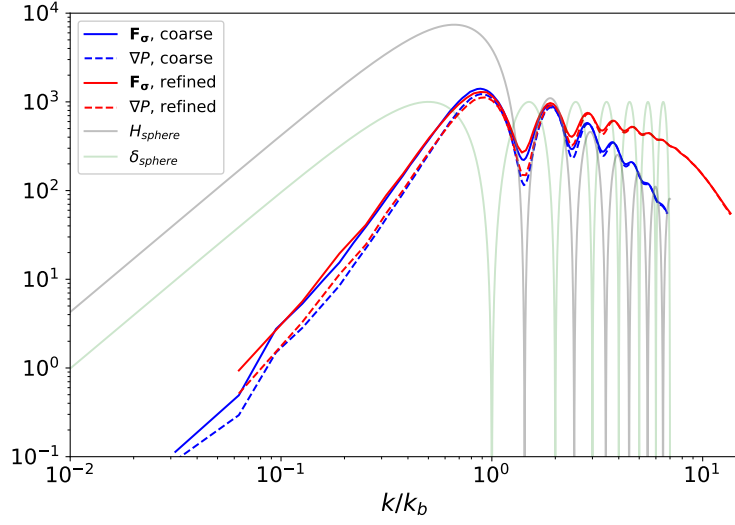


Figure 11: Normalized spectra $E_{\nabla P}$ of pressure gradient, and $E_{\mathbf{F}_\sigma}$ of interfacial force at $\alpha = 6\%$ (DNS results)

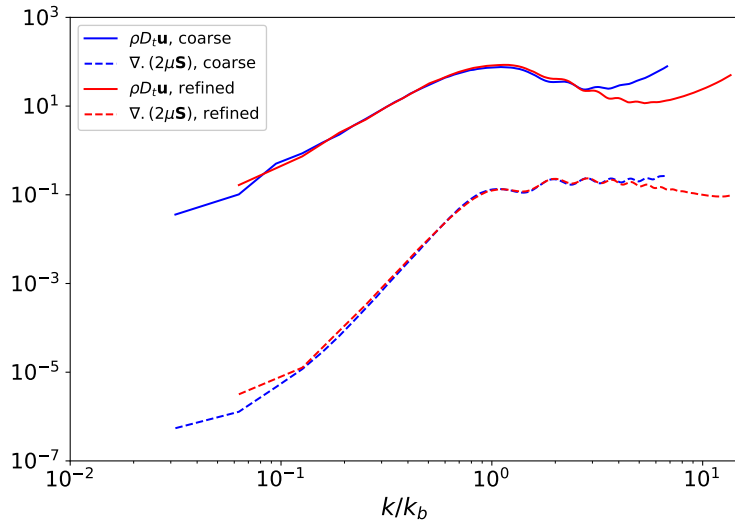


Figure 12: Normalized spectra $E_{\rho D_t \mathbf{u}}$ of inertia, and $E_{\nabla \cdot (2\mu \mathbf{S})}$ of viscous force at $\alpha = 6\%$ (DNS results)

521 pressure undergoes both a jump in its value and its derivative across the in-
 522 terface. So far, the spectra of the forces are in agreement with the theoretical
 523 predictions of section 3.

524 The spectra of the terms that explicitly involve the velocity, $-\rho D_t \mathbf{u}$ and
 525 $\nabla \cdot (2\mu \mathbf{S})$, show a somewhat different picture (fig. 12). Both are independent
 526 of the mesh refinement for $k/k_b < 3$ for $-\rho D_t \mathbf{u}$ and $k/k_b < 4$ for $\nabla \cdot (2\mu \mathbf{S})$.
 527 The fact that they show no oscillations while showing no decay in this range
 528 recalls the footprint of a Dirac-type singularity. As demonstrated earlier, these
 529 terms should not present such a singularity. That spectral behaviour at small
 530 scales is therefore a consequence of the approximation done by using a discrete
 531 description of the interface. Even if we are not able to relate the spectra of
 532 these two quantities to the detail of the numerical scheme, it is interesting to
 533 note that the small-scale plateaus reached by $E_{\rho D_t \mathbf{u}}$ and $E_{\nabla \cdot (2\mu \mathbf{S})}$ are lower than
 534 those of $E_{\nabla P}$ and $E_{\mathbf{F}_\sigma}$, suggesting that a part of the Dirac-like singularity of
 535 the latter two is redirected to the former two due to the approximate numerical
 536 treatment near the interface.

537 In summary, this section leads to the following conclusions. The spectral
 538 signature of the singularities is as predicted by theory for buoyancy, pressure
 539 gradient and interfacial force, but different for inertia and viscous force due to
 540 numerical approximations in the cells crossed by the interface. However, all
 541 spectra are remarkably independent of the mesh spacing, the effect of which
 542 is only significant at the small scales where the effect of singularities becomes
 543 dominant.

544 4.4. Energy budget in the spectral domain

545 The spectral energy balance of the kinetic energy of the two-phase mixture
 546 can be obtained in the same way as for a single-phase flow. The Fourier trans-
 547 form (eq. 10) of each term in the Navier-Stokes equation (eq. 4) is calculated,
 548 and contracted with the complex conjugate $\hat{\mathbf{u}}^*$ of the Fourier transform of the

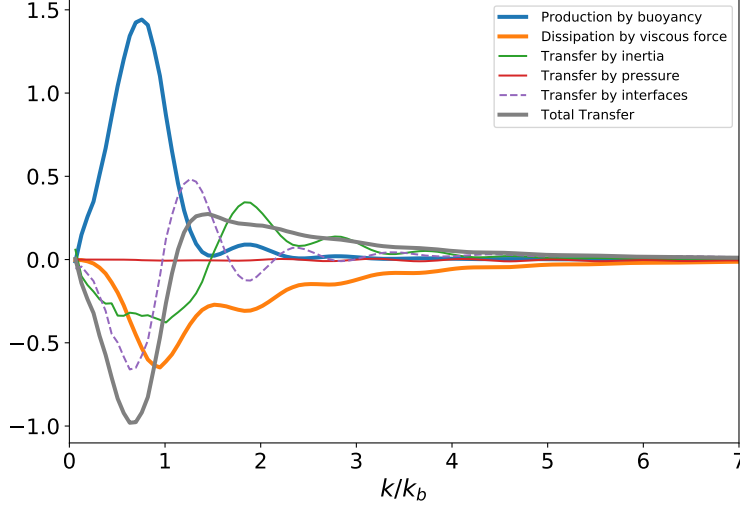


Figure 13: Normalized spectral density of the terms of the energy balance for the refined grid at $\alpha = 6\%$ (DNS results)

549 velocity:

$$\underbrace{+\widehat{\mu\nabla^2\mathbf{u}\cdot\hat{\mathbf{u}}^*}}_{\text{Dissipation}} + \underbrace{+(\widehat{\rho - \rho_m})\mathbf{g}\cdot\hat{\mathbf{u}}^*}_{\text{Production}} + \underbrace{-\widehat{\rho D_t\mathbf{u}\cdot\hat{\mathbf{u}}^*}}_{\text{Inertia}} + \underbrace{-\widehat{\nabla P}\cdot\hat{\mathbf{u}}^*}_{\text{Pressure}} + \underbrace{+\widehat{\mathbf{F}_\sigma}\cdot\hat{\mathbf{u}}^*}_{\text{Interfacial tension}} = 0. \quad (20)$$

Transfers

550 Each term is a complex-valued field in the wavenumber vector \mathbf{k} . We take its
 551 real part and integrate it over shells of constant $k = \|\mathbf{k}\|$ (eq. 11) to finally
 552 obtain a real-valued function of k . This means we will not be examining flow
 553 anisotropy in what follows.

554 Note that according to the Plancherel's theorem, each term \mathbf{T} of the momen-
 555 tum equation satisfies the relation: $\int \mathbf{T}(\mathbf{x})\cdot\mathbf{u}(\mathbf{x})dx^3 = \int \widehat{\mathbf{T}}(\mathbf{k})\cdot\widehat{\mathbf{u}}(\mathbf{k})^* dk^3$, which
 556 means that the integral over the wavenumbers of each term of the spectral bal-
 557 ance (eq. 20) is equal to the average power of \mathbf{T} . In particular, the first term
 558 can be expressed with the velocity spectrum as $\mu k^2 E_u$, and, its integral over
 559 k , noted $-\epsilon$, is equal to the dissipation rate of kinetic energy. It can thus be
 560 interpreted as the spectral density of the dissipation rate.

561 Since we are considering a statistical steady state, the integral over k of the

562 second term is equal to ϵ and corresponds to the rate of energy supplied to the
 563 system by external forces. The buoyancy term therefore represents the spectral
 564 density of the production rate of kinetic energy.

565 The integral over k of each of the three remaining terms is zero, which means
 566 that inertia, pressure and interfacial forces do not contribute to the total amount
 567 of power, their role being to transfer energy between scales. Note that it is only
 568 true in steady state.

569 Before examining the DNS results, it is useful to comment on a specificity
 570 of the inertia term when the densities of the two phases are different, as it
 571 was misinterpreted by one of the few previous works that dealt with such a
 572 situation (Pandey and Ramadugu, 2020). The inertia term can be split into
 573 two parts as $-\widehat{\rho D_t \mathbf{u}} \cdot \widehat{\mathbf{u}}^* = -\widehat{\rho \partial_t \mathbf{u}} \cdot \widehat{\mathbf{u}}^* - \widehat{\rho \mathbf{u} \cdot \nabla \mathbf{u}} \cdot \widehat{\mathbf{u}}^*$. When density is constant,
 574 ρ can be taken out of the Fourier-transform operator and the first term of the
 575 right-hand-side can be re-written $\partial_t(\frac{\widehat{\mathbf{u}} \cdot \widehat{\mathbf{u}}^*}{2})$, which is zero at steady state. On the
 576 other hand, when ρ is not constant, $-\widehat{\rho \partial_t \mathbf{u}} \cdot \widehat{\mathbf{u}}^*$ does not vanishes at steady state
 577 and contributes to the transfer of energy between the scales. It is important
 578 to stress that while $-\widehat{\rho D_t \mathbf{u}} \cdot \widehat{\mathbf{u}}^*$ is Galilean invariant (for $\|\mathbf{k}\| > 0$), the two
 579 parts of its decomposition are not. This is not a problem when ρ is constant,
 580 since we can always choose the reference frame where the average velocity is
 581 zero. However, it means that this decomposition is irrelevant in the present
 582 case involving two phases with different densities moving at different velocities.
 583 Pandey and Ramadugu (2020) adopted a different perspective. They decided
 584 to decompose the fluid acceleration term into a Eulerian time derivative and a
 585 convective part in a way so that the former term vanishes in steady state. For
 586 each term T of the Navier-Stokes equations, they defined its spectral density
 587 as: $\widehat{T} \cdot \widehat{\mathbf{u}}^* + \frac{\widehat{T}}{\rho} \cdot \widehat{\rho \mathbf{u}}$. The Eulerian time-derivative term is now written $\partial_t(\widehat{\rho \mathbf{u}} \cdot \widehat{\mathbf{u}}^*)$,
 588 which is indeed zero in steady state. However, this comes at a high price, as
 589 the physical meaning of terms involving \mathbf{T}/ρ is unclear. Moreover, the division
 590 by ρ strengthens singularities and their effect on the spectrum. What's more,
 591 their mathematical relevance is uncertain, in particular regarding \mathbf{F}^σ/ρ , which
 592 does not represent the interfacial stress jump and involves a ratio between the

593 Dirac and Heaviside distributions. We therefore see no advantage in adopting
594 this approach and use the classic method defined by eq. 20.

595 Figure 13 presents the spectral energy budget (eq. 20), where all spectra
596 have been normalized using k_b and ϵ . Oscillations with a period k_b of significant
597 amplitudes are visible on all terms, indicating that the singular parts are far
598 from being negligible.

599 The production term shows a large positive and almost symmetric peak
600 around $k = 0.75k_b$. Beyond $k = 1.5k_b$, it becomes a secondary term dominated
601 by oscillations of decaying amplitude. Between $k = 0$ and $1.5k_b$, production
602 is balanced by dissipation, inertia and interfacial tension. In contrast with
603 the turbulence of a single-phase flow, transfer here is ensured to a comparable
604 extent by inertia and interfacial force, while the role of the pressure gradient
605 remains negligible. However, the inertial and interfacial contributions exhibit
606 very strong oscillations, causing them to change sign and making it difficult
607 to understand them separately. The physical interpretation of the balance is
608 simplified if inertia, interfacial force and pressure gradient are added together
609 to construct the total transfer term, represented by the grey line in the figure.
610 This makes clear the existence of two regimes, both corresponding to an energy
611 transfer from large to small scales. Before the production peak ($0 \leq k \leq$
612 $0.75k_b$), the energy supplied by the work of buoyancy is mainly balanced by the
613 transfer term, which transports energy to smaller scales. After the dissipation
614 peak ($k \geq k_b$), the energy supplied from larger scales by the transfer term is
615 dissipated. This picture is close to single-phase flow turbulence, with the notable
616 difference that there is no scale separation between the peak of production
617 and the peak of dissipation, which explains the absence of a $k^{-5/3}$ inertial
618 subrange. It should also be noted that there is no subrange where production
619 and dissipation are in equilibrium, in contrast to what was postulated by Lance
620 and Bataille (1991) to explain the existence of the k^{-3} subrange. The same
621 conclusion was recently reached by Zamansky et al. (2024) who showed that
622 the k^{-3} subrange corresponds to a constant shear rate imposed by the bubble
623 wakes and may be explained by a mechanism of return to isotropy that takes

624 place once energy production by bubbles has ceased.

625 The total transfer possesses another property, which is of major interest
626 for the purpose of the present work. It has no oscillations, indicating that
627 the singularities of its three components cancel each other out, leaving only the
628 regular part. Since the sum of the production and dissipation terms balances the
629 transfer term, their singularities are the opposite of each other. It is therefore
630 sufficient to identify the singular part of one of them to obtain two distinct,
631 regular and singular spectral energy balances.

632 Since buoyancy acts on the bubble scale, it does not supply energy at scales
633 that are significantly smaller than R . Consequently, the regular part of the
634 production spectrum must decay very fast after k_b . The DNS spectrum plotted
635 in log scale in fig. 14a shows that the decay after the peak is interrupted by
636 strong oscillations on a power-law decaying baseline, which can be attributed
637 to the singular part. The regular part of the production spectrum can thus
638 be obtained by low-pass filtering of the DNS spectrum. This has been done
639 in fig. 14a, where the blue line shows the production spectrum multiplied by a
640 sharp filter, $\exp(-(k/k_c)^4)$, with $k_c = 1.3k_b$. (Changing the cutoff wavenumber
641 k_c , slightly changes the result in the vicinity of k_c , but has no effect beyond).
642 The singular part (grey dashed line), obtained as the difference between the total
643 spectrum and the regular part, combines several types of singularities since its
644 oscillations slowly evolves from a $\cos^2(kR)$ behavior to a $\sin^2(kR)$ behavior, and
645 its power decay from a slope -3 to -4 .

646 In contrast with production, the dissipation is only expected to experience a
647 viscous cutoff at scales much smaller than the bubbles, so there is no easy way
648 to distinguish between its singular and regular parts. Nevertheless, as noted
649 above, its singular part is the opposite of that of the production spectrum and
650 its regular part is obtained by subtracting it from the total dissipation spectrum.
651 Figure 14b shows a log plot of the total dissipation spectrum, as well as its
652 regular and singular parts obtained in that way. The regular part shows a clear
653 k^{-1} evolution in the range from $k = 0.8k_b$ (just after the production peak) to
654 $2-3 k_b$.

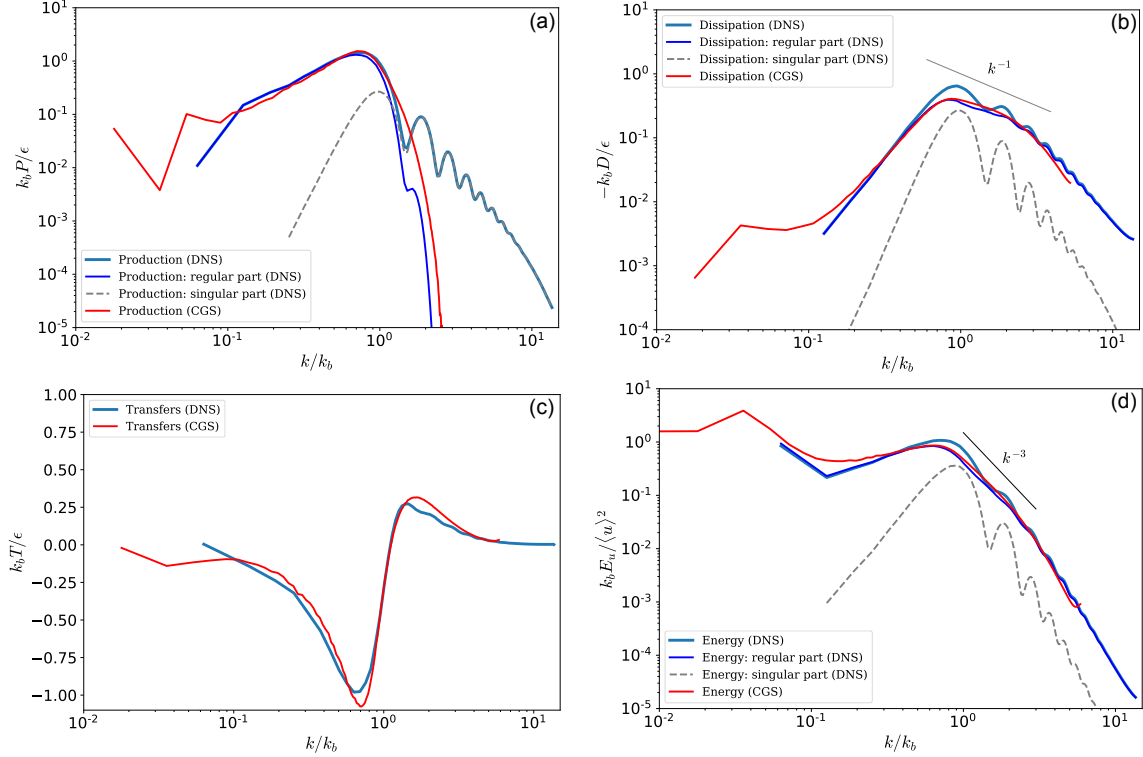


Figure 14: Normalized spectral density of the terms of the energy balance and energy spectrum. DNS at $\alpha = 6\%$ and CGS at $\alpha = 7.5\%$. (a): Production, (b): Dissipation, (c): Transfers, (d): Energy.

655 Provided the pressure gradient, inertia and interfacial contributions are con-
 656 sidered all together in a total transfer term, we eventually obtain two separate
 657 energy budgets, one for the regular part, the other for the singular part. The
 658 production (fig. 14a) and the dissipation (fig. 14b) involve both a regular and a
 659 singular part, while the total transfer (fig. 14b) is regular.

660 Finally, the singular and regular parts of the velocity spectrum are obtained
 661 by dividing the corresponding part of the dissipation spectrum by μk^2 . The
 662 regular part shows a k^{-3} evolution in the region where the dissipation spectrum
 663 shows a k^{-1} behavior.

664 **5. Comparison with Coarse-Grained simulations**

665 In this work, the Navier-Stokes equations have been directly solved without
 666 additional modelling and the effect of the singularities due to the presence of
 667 the interfaces have been filtered *a posteriori* out from the numerical results.
 668 An opposite approach is to filter the flow in the region close to the interfaces
 669 before solving the Navier-Stokes equations. In this case, all fields are regular.
 670 Such coarse-grained simulations (CGS) were introduced by Riboux et al. (2013)
 671 to model the agitation generated by a flow through an array of fixed bubbles
 672 and extended to simulate freely moving bubbles by Le Roy De Bonneville et al.
 673 (2021). The case of a homogeneous swarm of rising bubbles has been extensively
 674 investigated by this method in Zamansky et al. (2024), where a detailed analysis
 675 of the spectral energy budget was provided. In this section, we compare these
 676 CGS spectra to the DNS spectra presented in the previous section.

677 Here we briefly present the CGS simulations, focusing on elements that are
 678 useful for understanding the comparison with the DNS. A detailed description
 679 of the method is available in Le Roy De Bonneville et al. (2021); Zamansky
 680 et al. (2024). The carrying phase fills the entire domain without interruption.
 681 Its dynamics is described by the continuity and Navier-Stokes equations for
 682 an incompressible fluid of constant density and viscosity. The presence of the
 683 bubbles is accounted for in the Navier-Stokes equations by a forcing term $\mathbf{f}_{b \rightarrow f}$,

$$\mathbf{f}_{b \rightarrow f}(\mathbf{x}, t) = - \sum_{b=1}^{N_b} \mathbf{F}_{f \rightarrow b} G(\mathbf{x} - \mathbf{x}_b(t)), \quad (21)$$

684 where a Gaussian kernel,

$$G(\xi) = \frac{1}{(2\pi\sigma_G^2)^{3/2}} \exp\left(-\frac{\|\xi\|^2}{2\sigma_G^2}\right), \quad (22)$$

685 is used to distribute the force $-\mathbf{F}_{f \rightarrow b}$ exerted on the fluid by each bubble b . The
 686 location \mathbf{x}_b of each bubble is calculated by solving Newton's second law, where
 687 the force $\mathbf{F}_{f \rightarrow b}$ exerted by the fluid included drag, added-mass, buoyancy and
 688 Tchen forces, calculated by using classic expressions involving both the bubble
 689 velocity and the fluid velocity at the bubble location. The main difference

690 between the DNS and CGS approaches lies in the forcing added to the Navier-
 691 Stokes equations. In DNS, \mathbf{F}_σ is localized at the interfaces, while, in CGS, $\mathbf{f}_{b \rightarrow f}$
 692 is spread over a region of scale σ_G .

693 The CGS simulations have been carried out in a triperiodic cubic domain
 694 of dimension $L = 70d$, on a regular mesh of spacing $\Delta = d/15$. The spatial
 695 resolution is thus the same as that of the coarse DNS mesh, but the momentum
 696 supplied by the bubble is here filtered at a scale of the order of that of the
 697 bubble, since $2\sigma_G = 0.28d$. The physical parameters are those of air bubbles of
 698 diameter $d = 2.5$ mm rising in water. The results reported here correspond to a
 699 volume fraction $\alpha = 7.5\%$, and a bubble Reynolds number $Re = 760$.

700 The spectra are determined from the fluid pressure and velocity fields com-
 701 puted by the CGS. The spectral densities of energy (E_u) and dissipation ($\mu \nabla^2 \mathbf{u} \cdot \hat{\mathbf{u}}^*$)
 702 are obtained exactly as in the DNS. The buoyancy force is applied to the bub-
 703 bles, which then transfer it to the fluid through the momentum forcing $\mathbf{f}_{b \rightarrow f}$.
 704 The production spectrum is thus calculated from the work of the coupling force:
 705 $\widehat{\mathbf{f}_{b \rightarrow f} \cdot \hat{\mathbf{u}}^*}$. The spectral transfers are, as in a single-phase flow, ensured by iner-
 706 tia ($-\rho \widehat{D_t \mathbf{u} \cdot \hat{\mathbf{u}}^*}$) and pressure ($-\widehat{\nabla P \cdot \hat{\mathbf{u}}^*}$), with a vanishing contribution of the
 707 pressure in homogeneous flow condition.

708 Normalized CGS spectra have been reported in fig. 14 (red lines). Since ρ
 709 and μ are constant and the coupling force $\widehat{\mathbf{f}_{b \rightarrow f}}$ is smooth, CGS spectra do not
 710 have a singular part. The agreement between CGS spectra and the regular part
 711 of DNS spectra is remarkable and constitutes a cross-validation of both. On the
 712 one hand, the spreading of the momentum transferred from the bubble to the
 713 fluid over a region of comparable size to that of the bubble is confirmed to be
 714 significantly relevant, not only at scales larger than the filtering threshold, but
 715 also at significantly smaller scales. On the other hand, this gives us confidence in
 716 the method used to separate the regular and singular parts of the DNS spectra.

717 6. Conclusion

718 The spectral analysis of dispersed two-phase flows is complicated by the
719 presence of interfaces between the two phases, across which some quantities are
720 discontinuous. This difficulty can be circumvented by considering subdomains
721 containing only one of the two phases, but at the price of the severe limitation:
722 transfers of momentum and energy between phases cannot be described, making
723 it impossible to construct a spectral balance. Analyzing fields extending over
724 the entire domain is therefore a much more fruitful approach to understand the
725 physical mechanisms underlying the dynamics of turbulent fluctuations.

726 In the case of bubbles or droplets transported by a carrying phase, the com-
727 bination of jumps of density, viscosity and stresses across the interface leads
728 the various fields characterizing the dynamics of flow mixture to experience sin-
729 gularities, which can be ordered from the less to the most regular by means
730 of integer p : Dirac delta function ($p = -1$), Heaviside step function ($p = 0$),
731 discontinuity of the first derivatives ($p = 1$), discontinuity of the second deriva-
732 tives ($p = 2$)... It is important to stress that a given field has generally various
733 interfacial singularities. For example, the pressure gradient generally contains a
734 Dirac singularity caused by interfacial tension ($\kappa\sigma$) and a Heaviside singularity
735 caused by the jump in the gravity force ($\rho\mathbf{g}$). A field can be characterized by
736 its most severe singularity, p_{min} . The velocity field is generally continuous but
737 its derivatives are not, leading to $p_{min} = 1$.

738 The spectrum of any field combines a regular part, which represents the
739 smooth evolution outside the interface, and a singular part, which reflects inter-
740 facial singularities. At large wavenumbers, the spectrum of a singularity of order
741 p , follows a power-law decay as $-2p - 2$. Therefore there exists a wavenumber
742 above which, the spectrum of a physical field is dominated by its singular part,
743 and it ends up by being dominated by its most severe singularity, of order p_{min} .
744 The wavenumbers where the singular part begins to become significant depends
745 on the amplitude of the regular part relative to that of the singular part, and the
746 way it evolves with k . When the interfaces are the surface of droplets or bubbles,

747 the singular part of the spectrum reaches a maximum at a wavelength close to
 748 the droplet scale and follows a power-law at smaller scales. When the droplets
 749 are spheres of the same radius R , the spectrum of the singularities shows oscil-
 750 lations as $\sin^2(Rk + \phi)$, of period $k_b = \pi/R$. These oscillations vanish when the
 751 droplets are deformed or their size distributions is broad.

752 In a dispersed two-phase flow, the singular part of the spectra is therefore
 753 expected to be important for wavenumbers larger than k_b . For instance, it
 754 is insignificant on the major part of the turbulent spectra in the case of a
 755 turbulent flow laden with droplets of size smaller than the Kolmogorov micro-
 756 scale. However, it cannot be neglected when the droplet size is in the energetic
 757 wavelength range. In this work, we have investigated the case where its impact
 758 is the most important, a swarm of bubbles rising at a high Reynolds number,
 759 since the fluctuating energy is produced in a range around k_b . In addition,
 760 we have considered almost spherical bubbles of a single diameter d , for which
 761 the oscillations of the spectrum at a period k_b are a visible signature of the
 762 singular part. We also chose the same viscosity for the two phases to simplify
 763 the analysis.

764 A homogeneous rising swarm, at volume fractions $\alpha = 3\%$ and 6% and
 765 Reynolds number $Re = 500$, has been computed by Direct Numerical Simula-
 766 tions using a front tracking of the interfaces, with a mesh grid spacing $\Delta = d/14$
 767 or $d/27$. The conclusions reached are independent of α and Δ . The numeri-
 768 cal spectra of the velocity and of all the terms of the momentum equations
 769 clearly show the signature of singularities of order $p = -1$ (Dirac type), $p = 0$
 770 (Heaviside type) and $p \geq 1$ (continuous fields). Buoyancy, pressure gradient
 771 and interfacial forces show the singularities predicted by the theory. However,
 772 the two terms that explicitly imply velocity, namely inertia and viscous forces,
 773 are less regular than they should be. This indicates that, even though the mo-
 774 mentum balance is locally satisfied everywhere, the numerical treatment in the
 775 meshes that are crossed by an interface, redistributes the singularities between
 776 the different terms, leading to a less regular velocity field.

777 The spectral power densities of all the forces contributing to the energy bal-

778 ance were determined, in the same way as usually done in turbulence studies.
779 This budget is made of five terms. The buoyancy term corresponds to the pro-
780 duction of kinetic energy. The viscous term corresponds to the dissipation of
781 kinetic energy into heat. The integral over the wavenumbers of the production
782 term is the opposite of that of the dissipation term and equal to the dissi-
783 pation rate of energy ϵ . The inertia, interfacial tension and pressure-gradient
784 terms transfer energy between scales without contributing to the total amount
785 of power. It turns out that the singular part cancels out when we add the three
786 transfer terms together, leading to a regular total transfer term. Then, taking
787 advantage of the fact that the regular part of the production term decreases
788 very sharply beyond k_b , its singular and regular parts can be separated. Since
789 the singular part of the dissipation term must balance the singular part of the
790 production term, we end up with two separate budgets, one for the regular
791 part, one for the singular part. These results have been compared with those
792 of Coarse-Grained Simulations, in which the momentum transfer between the
793 bubbles and the fluid are filtered before the Navier-Stokes equations are solved.
794 The CGS spectra are found to be in remarkable agreement with the regular part
795 of the DNS spectra, validating both approaches to obtain the regular part of
796 the spectra.

797 This work proves that it is relevant to analyze DNS spectra of bubbly flows
798 computed by considering the fields over the entire domain. In the case of homo-
799 geneous bubble-induced agitation, it has been possible to separate the regular
800 and singular parts of the spectral energy budget thanks to the two following
801 properties: (1) the singular parts of the transfer terms cancels out when we add
802 them, and (2) the production term decay very sharply after k_b . The question
803 now is under which conditions these two properties are valid. In a future work,
804 we shall address the case of coupled forced isotropic homogeneous turbulence
805 and bubble-induced agitation.

806 **Acknowledgement**

807 This work was granted access to the HPC resources of TGCC under the
808 allocation 2023-A0142B07712 made by GENCI.

809 For the purpose of Open Access, a CC-BY public copyright licence has been
810 applied by the authors to the present document and will be applied to all sub-
811 sequent versions up to the Author Accepted Manuscript arising from this sub-
812 mission.

813 **References**

814 E. Alméras, Varghese Mathai, Detlef Lohse, and F Toschi. Experimental in-
815 vestigation of the turbulence induced by a bubble swarm rising within in-
816 cident turbulence. Journal of Fluid Mechanics, 825:1091–1112, 2017. doi:
817 10.1017/jfm.2017.410.

818 E. Bacry, J. F. Muzy, and A. Arnéodo. Singularity spectrum of fractal signals
819 from wavelet analysis: Exact results. Journal of Statistical Physics, 70(3-4):
820 635–674, 1993. doi: 10.1007/BF01053588.

821 S Balachandar and J K Eaton. Turbulent Dispersed Multiphase Flow. Annual
822 Review of Fluid Mechanics, Vol 43, 42(1):111–133, 2010. doi: 10.1146/
823 annurev.fluid.010908.165243.

824 L. Brandt and F. Coletti. Particle-Laden Turbulence: Progress and Perspec-
825 tives. Annual Review of Fluid Mechanics, 54(1):159–189, January 2022. ISSN
826 0066-4189, 1545-4479. doi: 10.1146/annurev-fluid-030121-021103.

827 H. Broer and F. Takens. Mixed spectra and rotational symmetry. Archive
828 for Rational Mechanics and Analysis, 124(1):13–42, 1993. doi: 10.1007/
829 BF00392202.

830 M. Cialesi-Esposito, M. E. Rosti, S. Chibbaro, and L. Brandt. Modulation
831 of homogeneous and isotropic turbulence in emulsions. Journal of Fluid
832 Mechanics, 940:A19, 2022. doi: 10.1017/jfm.2022.179.

- 833 M. S Dodd and A. Ferrante. On the interaction of Taylor length scale size
834 droplets and isotropic turbulence. Journal of Fluid Mechanics, 806:356–412,
835 November 2016. doi: 10.1017/jfm.2016.550.
- 836 A du Cluzeau, G Bois, and A Toutant. Analysis and modelling of Reynolds
837 stresses in turbulent bubbly up-flows from direct numerical simulations.
838 Journal of Fluid Mechanics, 866:132–168, 2019. doi: 10.1017/jfm.2019.100.
- 839 A. du Cluzeau, G. Bois, N. Leoni, and A. Toutant. Analysis and model-
840 ing of bubble-induced agitation from direct numerical simulation of homo-
841 geneous bubbly flows. Physical Review Fluids, 7(4):044604, 2022. doi:
842 10.1103/PhysRevFluids.7.044604.
- 843 B. Dubrulle. Beyond kolmogorov cascades. Journal of Fluid Mechanics, 687:
844 P1–63, 2019. doi: doi:10.1017/jfm.2019.98.
- 845 J. Duchon and R. Robert. Inertial energy dissipation for weak solutions of
846 incompressible euler and navier-stokes equations. Nonlinearity, 13(1):249,
847 2000.
- 848 A. Freund and A. Ferrante. Wavelet-spectral analysis of droplet-laden isotropic
849 turbulence. Journal of Fluid Mechanics, 875:914–928, 2019. doi: 10.1017/
850 jfm.2019.515.
- 851 I. M. Gelfand and G. E. Shilov. Generalized Functions Vol 1 Properties And
852 Operations. Academic Press - New York and London, 1964.
- 853 A. Innocenti, A. Jaccod, S. Popinet, and S. Chibbaro. Direct numerical simu-
854 lation of bubble-induced turbulence. Journal of Fluid Mechanics, 918, 2021.
855 doi: 10.1017/jfm.2021.288.
- 856 I. Kataoka. Local instant formulation of two-phase flow. International
857 Journal of Multiphase Flow, 12(5):745–758, September 1986. doi: 10.1016/
858 0301-9322(86)90049-2.

- 859 B. Lalanne, L. Villegas Rueda, S. Tanguy, and F. Risso. On the computation
860 of viscous terms for incompressible two-phase flows with Level Set/Ghost
861 Fluid Method. Journal Of Computational Physics, 301:289–307, 2015. doi:
862 10.1016/j.jcp.2015.08.036.
- 863 M Lance and J Bataille. Turbulence in the liquid-phase of a uniform bubbly air
864 water-flow. J. Fluid Mech., 222(-1):95–118, January 1991.
- 865 M. Le Berre, T. Lehner, and Y. Pomeau. Singularities in turbulent flows: How
866 to observe them? Physica D: Nonlinear Phenomena, 443:133563, 2023.
- 867 F. Le Roy De Bonneville, R. Zamansky, F. Risso, A. Boulin, and J.-F. Haquet.
868 Numerical simulations of the agitation generated by coarse-grained bubbles
869 moving at large Reynolds number. Journal of Fluid Mechanics, 926:A20, 2021.
870 doi: 10.1017/jfm.2021.670.
- 871 F. Lucci, A. Ferrante, and S. Elghobashi. Modulation of isotropic turbulence
872 by particles of Taylor length-scale size. Journal of Fluid Mechanics, 650:5–55,
873 2010. doi: 10.1017/S0022112009994022.
- 874 J Martínez Mercado, D Chehata G, D Van Gils, C Sun, and D Lohse. On
875 bubble clustering and energy spectra in pseudo-turbulence. J. Fluid Mech.,
876 650:287–306, March 2010.
- 877 S Mendez-Diaz, J C Serrano-García, R Zenit, and J A Hernández-Cordero.
878 Power spectral distributions of pseudo-turbulent bubbly flows. Phys Fluids,
879 25(4):043303, 2013.
- 880 L. Onsager. Statistical hydrodynamics. Il Nuovo Cimento, 6(2):279–287, 1949.
- 881 V. Pandey and P. Ramadugu, R.and Perlekar. Liquid velocity fluctuations and
882 energy spectra in three-dimensional buoyancy-driven bubbly flows. Journal
883 of Fluid Mechanics, 884:R6, February 2020. doi: 10.1017/jfm.2019.991.
- 884 V. Pandey, D. Mitra, and P. Perlekar. Turbulence modulation in buoyancy-
885 driven bubbly flows. Journal of Fluid Mechanics, 932:A19, February 2022.
886 ISSN 0022-1120, 1469-7645. doi: 10.1017/jfm.2021.942.

- 887 A. S. Pikovsky, M. A. Zaks, U. Feudel, and J. Kurths. Singular continuous
888 spectra in dissipative dynamics. Physical Review E, 52(1):285–296, 1995.
889 doi: 10.1103/PhysRevE.52.285.
- 890 S. B. Pope. Turbulent Flows. Cambridge University Press, 2000.
- 891 V N Prakash, J Martínez Mercado, L van Wijngaarden, E Mancilla, Y Tagawa,
892 D Lohse, and C Sun. Energy spectra in turbulent bubbly flows. J. Fluid
893 Mech., 791:174–190, February 2016.
- 894 G Riboux, F Risso, and D Legendre. Experimental characterization of the
895 agitation generated by bubbles rising at high Reynolds number. J. Fluid
896 Mech., 643:509–539, January 2010.
- 897 G. Riboux, D. Legendre, and . Risso. A model of bubble-induced turbulence
898 based on large-scale wake interactions. Journal of Fluid Mechanics, 719:362–
899 387, 2013. doi: 10.1017/jfm.2013.12.
- 900 F Risso. Theoretical model for k^{-3} spectra in dispersed multiphase flows. Phys
901 Fluids, 23(1):011701, 2011.
- 902 F. Risso. Agitation, Mixing, and Transfers Induced by Bubbles. Annual Review
903 of Fluid Mechanics, Vol 43, 50(1):25–48, 2018.
- 904 I Roghair, J M Mercado, M Van Sint Annaland, H Kuipers, C Sun, and D Lohse.
905 Energy spectra and bubble velocity distributions in pseudo-turbulence: Nu-
906 merical simulations vs. experiments. Int. J. Multiph. Flow, 37(9):1093–1098,
907 2011.
- 908 G Tryggvason, Bernard Bunner, and Gretar Tryggvason. Dynamics of homoge-
909 neous bubbly flows Part 2. Velocity fluctuations. Journal of Fluid Mechanics,
910 466(0):53–84, 2002. doi: 10.1017/S0022112002001180.
- 911 R Zamansky, F Le Roy De Bonneville, and F Risso. Turbulence induced by
912 a swarm of rising bubbles from coarse-grained simulations. Journal of Fluid
913 Mechanics, 984:A68, 2024. doi: doi:10.1017/jfm.2024.230.